On the necessity of modelling fluid–structure interaction for stented coronary arteries

Claudio Chiastra[a], *Francesco Migliavacca*[a], *Miguel Ángel Martínez*[b,c], *Mauro Malvè*[b,c,d,*]

[a]*Laboratory of Biological Structure Mechanics (LaBS), Department of Chemistry, Materials and Chemical Engineering "Giulio Natta", Politecnico di Milano, Italy*

[b]*Aragón Institute of Engineering Research (I3A), Universidad de Zaragoza, C/María de Luna s/n, E-50018 Zaragoza, Spain*

[c]*Centro de Investigación Biomédica en Red-Bioingeniería Biomateriales y Nanomedicina (CIBER-BBN), C/Poeta Mariano Esquillor s/n, E-50018 Zaragoza, Spain*

[d]*Universidad Pública de Navarra, Departamento de Ingeniería Mecánica, Energética y de Materiales, Campus Arrosadía, E-31006 Pamplona, Spain*

Received 30 September 2013 Received in revised form
23 January 2014
Accepted 5 February 2014 Available online 12 February 2014

*Corresponding author at: Public University of Navarra, Department of Mechanical Engineering, Energetics and Materials, Campus Arrosadía, 31006 Pamplona, Spain. Tel.: +34 948 16 9294; fax: +34 948 16 9099.

E-mail address: mauro.malve@unavarra.es (M. Malvè).

1. Introduction

Among the percutaneous interventions, stenting is the most commonly performed procedure for the treatment of coronary atherosclerotic lesions; however, serious clinical complications remain such as in-stent restenosis (ISR), which is the reduction in lumen size following the stent implantation (Park et al., 2012). The primary process leading to ISR is neointimal hyperplasia (NH) that consists in an excessive growth of tissue in and around the implanted stent, resulting in a decreased blood flow through the vessel. One of the stimuli to NH is the altered hemodynamics due to the stent presence that causes abnormal shear stresses on the endothelial cells (Wentzel et al., 2008).

To date, numerical models have been established as a valid tool for studying the local hemodynamics of stented vessels, allowing the calculation of the wall shear stress (WSS), which is otherwise difficult to be measured *in vivo*. Many computational fluid dynamic (CFD) studies have been proposed in the literature, considering idealized (Gundert et al., 2013, 2012, Murphy and Boyle, 2010a, Pant et al., 2010) or more complex image-based stented coronary models (Chiastra et al., 2013, Ellwein et al., 2011, Gundert et al., 2011). Despite providing a great deal of information, in these fluid dynamic models the arterial wall and the stent are considered rigid and fixed, an assumption that may influence the WSS and flow pattern results. In the recent past the fluid–structure interaction (FSI) approach has been applied to a wide range of arterial problems including the aorta (Figueroa et al., 2006), abdominal aortic aneurysms (Leung et al., 2006; Scotti et al., 2008; Scotti and Finol, 2007; Tezduyar et al., 2007; Wolters et al., 2005), cerebral aneurysms (Gerbeau et al., 2005; Takizawa et al., 2012, 2011; Tezduyar et al., 2007), carotid artery bifurcations (Filipovic et al., 2013; Gao et al., 2009; Gerbeau et al., 2005; Lee et al., 2012; Perktold and Rappitsch, 1995; Tezduyar et al., 2007), and anastomoses of bypass grafts (Hofer et al., 1996; Leuprecht et al., 2002). The extensive study of Tang and coworkers on human carotid atherosclerotic plaque (Tang et al., 2008, 2004, 2001, 1999, Teng et al., 2010, Yang et al., 2011, 2010) deserves special mentioning. Indeed, they provided structural and hemodynamics markers for the initiation and development of atherosclerosis in carotid arteries using the FSI approach. In a further study Belzacq et al. (2012) investigated the effect of the length, the stiffness, and the severity of an asymmetric carotid atherosclerotic plaque on the mechanical action of the blood flow by developing a parametric FSI model.

FSI simulations of coronary artery models have been performed only in a limited number of studies, without considering the presence of stents. Koshiba et al. (2007) simulated blood flow, arterial wall deformation and filtration flow in the wall of a coronary artery with multiple bends. The results of the FSI simulation were used to analyze the low density lipoproteins transport in the arterial lumen and wall by solving the advection–diffusion–reaction equation. Yang et al. (2009) developed a FSI model of the middle segment of the human right coronary artery (RCA) with atherosclerotic plaques, based on intravascular ultrasound (IVUS) images, in order to quantify the effects of anisotropic vessel properties and cyclic bending of the coronary plaque on flow and plaque stress/strain conditions. A similar study was recently conducted by Asanuma et al. (2013) who investigated the distributions of shear stress and tissue stresses in the proximal segment of a stenotic human left anterior descending coronary artery (LCA). Torii et al. (2009) performed a FSI analysis of a human stenotic RCA using physiological velocity and pressure waveforms to investigate the effects of wall compliance on hemodynamics. A comparison between a FSI and a rigid-wall model was carried out showing noticeable differences in instantaneous WSS profiles. Finally, Malvè et al. (2012) made a comparison between the WSS distribution of a compliant and a rigid-wall model of a human left main coronary artery with its main branches. WSS distributions were substantially affected by the arterial wall compliance, in particular considering the minimum and maximum values of WSS.

The aim of the present work is to perform FSI analyses of a stented coronary artery in order to understand the effects of the wall compliance on hemodynamic quantities. Both a bare-metal (cobalt–chromium – CoCr) and a polymeric (poly-L-lactide – PLLA) stent are considered. The choice of the polymeric stent, with the same design of the metallic one, is done because of the different stiffness of the device, which could produce bigger deformations with a great influence on the fluid dynamics. The results of the FSI and the corresponding rigid-wall models are then compared, focusing in particular on the analysis of the WSS distribution.

2. Materials and methods

2.1. Geometry

A geometrical model of a straight coronary artery and a typical open-cell stent were created using the CAD software RHINOCEROS v.4.0 Evaluation (McNeel & Associates, Indianapolis, IN, USA). The geometry of the artery was created with a length of 20 mm, an internal diameter of 2.7 mm and an arterial wall thickness of 0.9 mm. The stent model is characterized by eight rings with a total length of 8.5 mm, an external diameter of 1.55 mm (uncrimped configuration) and strut thickness of 90 μm.

In order to obtain the geometrical model of a stented artery which is not based only on geometrical assumptions but also takes into account the deformation of the vessel caused by the stent deployment, the device was expanded inside the vessel through a structural analysis reaching the final diameter of 3 mm. The simulation was carried out by means of ABAQUS/Explicit (Dassault Systemes, Simulia Corp., RI, USA) following the method proposed in Gastaldi et al. (2010).

The final geometrical configuration, after the elastic recoil, was exported as a triangulated surface and used to create the fluid and solid domains for the subsequent FSI and CFD analyses (Morlacchi et al., 2011). An extension with a length of four diameters (10.8 mm) was added at both extremities of the arterial model (Fig. 1a) in order to obtain developed flow near the region of the stent and avoid border effects due to

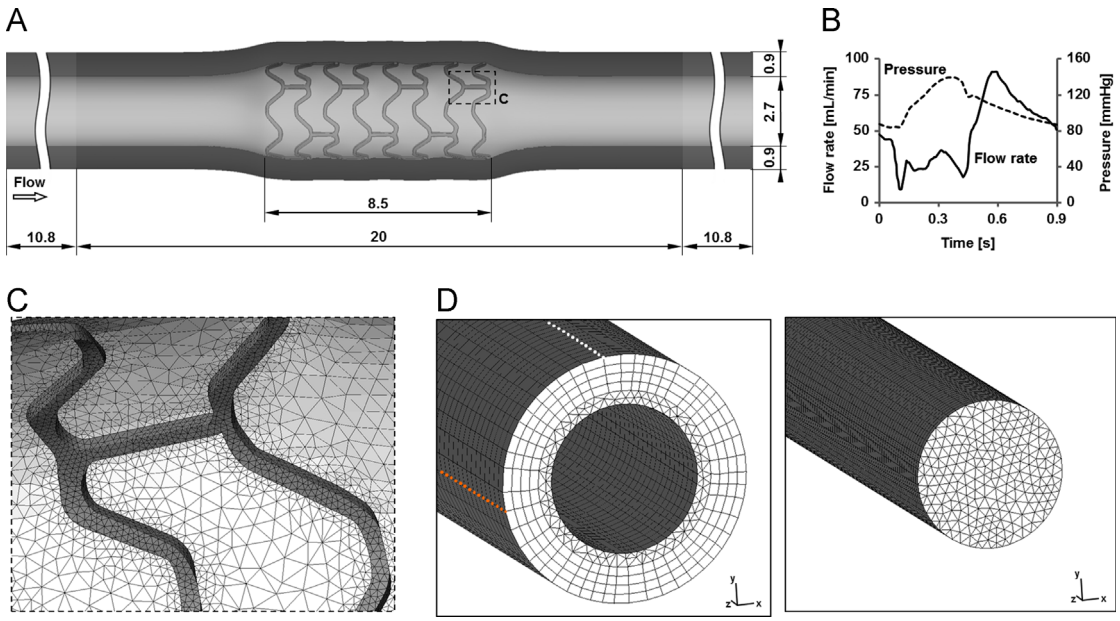

Fig. 1 – (A) Geometrical model of the straight coronary artery with a typical deployed open-cell stent. The geometry was obtained through a structural simulation of stent expansion inside the vessel. Extensions with a length of four diameters were added at the extremities of the model. The fluid domain is displayed in light gray while the solid domain in dark gray. Dimensions are in millimeters. (B) Flow rate and pressure waveforms of a human LAD (Davies et al., 2006) applied at the inlet and at the outlet cross-section of the model, respectively. Peak pressure is at $t=0.37$ s while peak flow is at $t=0.59$ s. (C) Detail of the tetrahedral grid obtained at the fluid-structure interface in the vicinity of the stent struts. The mesh is characterized by smaller elements close to the struts. (D) Particular of the mesh of the solid (left) and the fluid (right) domain at one extremity of the extensions (inlet cross-section). The solid domain is discretized by prismatic elements with triangular base in the inner part and by a layer of prismatic elements with rectangular base in the external part. The dots aligned with the z-axis indicate the constrains which were added in the extended regions to avoid the motion of the vessel outside its axis during the cardiac cycle. For the set of nodes in x direction (orange dots), movement in y direction was not allowed while for the set of nodes in y direction (white dots), movement in x direction was not allowed. (For interpretation of the references to color in this figure legend, the reader is referred to the web version of this article.)

the constrains in the inlet and outlet cross-sections, thus reducing their influence on the results.

2.2. *Numerical grids*

The geometry of the artery is complex in the vicinity of the stent struts making the compatibility between the fluid and solid domains critical during a FSI simulation. To minimize this problem, the two domains were discretized simultaneously obtaining coincident nodes at the fluid–structure interface.

The meshing software ANSYS ICEM CFD v.14.0 (ANSYS Inc., Canonsburg, PA, USA) was used. An unstructured tetrahedral mesh was generated in the fluid domain using smaller elements close to the struts (Fig. 1c) as previously done in Chiastra et al. (2012). The fluid grid, which was chosen after an appropriate mesh independence study, had 1,121,130 elements (222,476 nodes).

In the solid domain an unstructured hybrid tetrahedral and prismatic grid was created (Fig. 1d). In particular, the stent and the inner part of the arterial wall were meshed with tetrahedral elements because of the complexity of the geometry and the necessity of obtaining coincident nodes between the fluid and solid domains. The external part of the arterial wall was meshed with a layer of prismatic elements. This choice allowed us to create elements oriented in the radial direction of the vessel, with an optimal quality (determinant criteria close to 1). The total number of elements was also reduced with respect to a pure tetrahedral grid. In particular, the mesh contained 899,710 elements (189,521 nodes). The final solid mesh is finer than that obtained after an independence study performed on the artery without stent. In fact, the device adds complexity to the geometry and needs to be correctly refined.

The Octree method was chosen for the creation of the tetrahedral meshes for both the domains. This method ensures refinement of the mesh where necessary, but maintains larger elements where possible. For the solid domain a full tetrahedral mesh was initially created, prisms were then created by extrusion of the surface mesh, and the resulting prisms were made conformal with the existing tetrahedral volume mesh.

2.3. *Material properties*

The arterial wall was modeled as a hyperelastic incompressible isotropic and homogeneous material. The following strain energy function was considered:

$$W = A[\exp(B(\bar{I}_1 - 3)) - 1] + U(J) \tag{2.1}$$

where $\bar{I}_1$ is the first invariant of the deviatoric right Cauchy-Green tensor $\bar{C} = J^{-2/3}F^TF$, $J = \det(F)$ is the Jacobian, F is the standard deformation gradient, U is the volumetric energy function and A and B are the material constants, which were set to 3.71 Pa and 140.2, respectively. This strain energy function was first proposed by Demiray (1972), and later used by Delfino et al. (1997) for a carotid artery bifurcation model and Rodriguez et al. (2008) for an abdominal aortic aneurysm model. The function parameters were fitted using the experimental tests of human coronary arteries obtained by Carmines et al. (1991). This material modeling was successfully applied to a coronary artery in a previous study (Malvè et al., 2012). This model takes into account the effect of the axial pre-stretch since the used experimental data also included it. The viscoelasticity, the active behavior of muscle fibers of the artery, and the intrinsic anisotropy, due to the preferential directions of collagen and muscle fibers, were neglected. This assumption might alter the results obtained for the structural part in terms of stresses and strains, but does not alter the overall compliance of the artery in presence of the stent due to the fact that the material model used for the artery fitted experimental data and provide the same stiffness. Since the aim of the work is the analysis of the compliant artery and not the evaluation of the stresses inside it, in first approximation the results have to be considered acceptable.

The stent material was considered linear elastic, isotropic and homogeneous. Two different cases were analyzed maintaining the same geometry: CoCr (Young's modulus=233 GPa and Poisson's ratio=0.35) and PLLA stent (Young's modulus=900 MPa and Poisson's ratio=0.30).

Relative displacements were not allowed between the stent and the arterial wall. In fact, the volume was meshed with coincident nodes at the interface between the stent and the arterial wall. Although non-physiological, this condition allowed a significant reduction in the complexity of the model.

The blood was modeled as an incompressible Newtonian fluid, with a density of 1060 kg/m^3 and a dynamic viscosity of 0.0035 Pa s (Rikhtegar et al., 2013). Since the Reynolds number based on the inlet diameter was 210 at peak of flow rate, an order of magnitude smaller than the Reynolds number for transition to turbulence (2300) (Spurk and Aksel, 2008), the flow was assumed to be laminar under unsteady conditions. The Womersley number was 1.95.

2.4. Boundary and flow conditions

The extremities of the extensions of the solid model were constrained by preventing rigid-body axial and transaxial motion. The constrains were applied far from the stented region, at a distance longer than four diameters (Fig. 1a). Therefore, the influence of these conditions on the stented region is very limited. In order to avoid the motion of the vessel outside of its axis (z-axis) during the cardiac cycle, constrains were added in x and y direction to sets of nodes along the length of the extensions (Fig. 1d). In particular, along the extensions, starting from the top and bottom surfaces, for the nodes set in x direction (Fig. 1d – orange dots), the movement in y direction was not allowed while, for the nodes set in y direction (Fig. 1d – white dots), the movement in x direction was not allowed. These conditions are widely used for FSI biomechanical studies of coronary arteries (Malvè et al., 2012; Torii et al., 2009), abdominal aneurisms (Scotti et al., 2008; Takizawa et al., 2011, Torii et al., 2010, 2006) and carotid arteries (Malvè et al., 2014).

The artery was initially pressurized by applying at the inlet cross-section a ramp of velocity from 0 m/s to 0.138 m/s and, at the outlet, a ramp of pressure from 0 mmHg to 80 mmHg. Then, the velocity and pressure waveforms measured by Davies et al. (2006) in a human left coronary artery were imposed (Fig. 1b) at the inlet and the outlet, respectively. The conditions were assumed to be uniform over the cross-section. The average flow rate was 45 mL/min and the duration of the cardiac cycle was 0.9 s.

The no-slip boundary condition was applied to the fluid-structure interface (surface representing the endothelial wall and the stent struts).

2.5. Numerical simulations

The following four analyses were performed: FSI and rigid-wall simulation of the arterial model with the CoCr stent, and FSI and rigid-wall simulation of the model with the PLLA stent. All the simulations were carried out using the commercial finite element package ADINA v.8.7.3 (ADINA R&D, Inc., Watertown, MA, USA).

2.5.1. FSI simulations

Fully coupled FSI simulations were performed. The numerical approach uses the arbitrary Lagrangian–Eulerian (ALE) formulation (Bathe and Zhang, 2004; Bathe et al., 1999) for the fluid domain and a typical Lagrangian formulation of the solid domain (Bathe and Zhang, 2004; Donea et al., 1982).

Considering the moving reference velocity, the Navier–Stokes equation can be written as:

$$\rho_F \frac{\partial \mathbf{v_F}}{\partial t} + \rho_F((\mathbf{v_F} - \mathbf{w}) \cdot \nabla)\mathbf{v_F} = -\nabla p + \mu \nabla^2 \mathbf{v_F} + \mathbf{f_F^B} \tag{2.2}$$

where the term $\mathbf{w}$ is the moving mesh velocity vector, $\mathbf{v_F}$ is the velocity vector, p is the pressure, $\mathbf{f_F^B}$ is the body force per unit volume, ρ_F is the fluid density, and μ is the dynamic viscosity. In the ALE formulation, $(\mathbf{v_F} - \mathbf{w})$ is the relative velocity of the fluid with respect to the moving coordinate velocity.

The governing equation of the solid domain is the following momentum conservation equation:

$$\nabla \cdot \boldsymbol{\sigma_S} + \mathbf{f_F^B} = \rho_S \ddot{\mathbf{u}}_\mathbf{S} \tag{2.3}$$

where ρ_S is the solid density, $\boldsymbol{\sigma_S}$ is the solid stress tensor, $\mathbf{f_F^B}$ is the body force per unit volume and $\ddot{\mathbf{u}}_\mathbf{S}$ is the local acceleration of the solid. The domains described by Eqs. 2.2 and 2.3 are then coupled through displacement compatibility and traction equilibrium (Bathe and Zhang, 2004) with the following equations:

$$\mathbf{u_S} = \mathbf{u_F} \qquad (x, y, z) \in \Gamma^F_{wall} \cap \Gamma^S_{wall} \tag{2.4}$$

$$\boldsymbol{\sigma_S} \cdot \mathbf{n_S} + \boldsymbol{\sigma_F} \cdot \mathbf{n_F} = 0 \qquad (x, y, z) \in \Gamma^F_{wall} \cap \Gamma^S_{wall} \tag{2.5}$$

where Γ^F_{wall} and Γ^S_{wall} are the boundaries of the fluid and solid domains, respectively. Eq. 2.5 is an equilibrium condition

between the stresses acting in normal direction on both domain boundaries Γ^{F}_{wall} and Γ^{S}_{wall}.

The governing equations were solved with the finite element method, which discretizes the computational domain into finite elements that are interconnected by element nodal points. For the structural model, a sparse matrix solver was used to solve the system. The full Newton–Raphson method (Bathe, 2006a) with a maximum of 500 iterations in each time step was chosen as iteration scheme.

The fluid domain employs special flow-condition-based-interpolation (FCBI-C) tetrahedral elements (Bathe, 2006b). All solution variables are defined in the center of the element and the coupling between the velocity and the pressure is handled iteratively. FCBI-C elements require the segregated method to solve the nonlinear equations. The sparse linear equation solver based on Gaussian elimination was used. To solve the coupling between the fluid and the structural models, the iterative method was chosen (Bathe, 2006b). In this computing method, the fluid and solid solution variables are fully coupled. The fluid equations and the solid equations are solved individually in succession, always using the latest information provided from another part of the coupled system. This iteration is continued until convergence in the solution of the coupled equations is reached. The maximum number of fluid-structure iterations for each time step was set to 1000. The time step size was set to 0.001 s (900 time steps were necessary for one cardiac cycle).

Simulations were performed in parallel on one node of a cluster with an Intel processor, 8 CPUs, with a CPU speed of 2268 MHz and a total memory of 24 Gb. One cardiac cycle was modeled. In order to verify that one cardiac cycle was enough to guarantee correct results, the CoCr FSI model and the corresponding rigid-wall model were investigated by simulating three cardiac cycles. No significant differences were found in the WSS results between the first and the third cardiac cycle. It has to be noted that the calculation time of the FSI simulation was around 500 h for one cardiac cycle.

2.5.2. *Rigid-wall simulations*

The same settings chosen for the fluid domain of the FSI models were used. In order to obtain a more realistic comparison between FSI and rigid-wall simulations, the geometries of the CoCr and PLLA cases, pressurized at 80 mmHg, were considered. More in detail, the structural model of the stented artery, for both cases, PLLA and CoCr, is initially not pressurized. For this reason, before a cardiac cycle can be applied, the diastolic pressure has to be reached. In order to start the heart cycle with identical geometrical configurations and properly perform a comparison of hemodynamics variables between rigid-wall and FSI simulations, the reference diastolic configuration of the artery was considered for the rigid-wall analyses. By means of the commercial software MATLAB (MathWorks Inc. – Natick, MA, USA), the deformed mesh obtained from the FSI simulation at the beginning of the cardiac cycle was used to generate an input grid for the CFD computations. This mesh allows that the performed simulations, rigid-wall and FSI analyses, could be compared taking into account only the compliance of the arterial wall due to the cardiac cycle.

In Fig. 2 the comparison between the initial undeformed configuration and the diastolic configuration of the CoCr and PLLA models is presented.

2.6. *Results quantification*

For the FSI cases, the displacements of the fluid–structure interface during the cardiac cycle were analyzed. Moreover, four different cross-sections (S1, S2, S3, and S4) were chosen to evaluate the variation of area and the corresponding diameter (Fig. 3). The area variation (A_{pp}–A_{lp}) expressed in percentage was calculated as:

$$\text{Area variation } [\%] = \frac{A_{pp} - A_{lp}}{A_{lp}} 100 \tag{2.6}$$

where A_{pp} is the area of the cross-section at peak pressure and A_{lp} is the area of the cross-section at the minimum pressure during the cardiac cycle.

The diameter variation ($d_{pp} - d_{lp}$) expressed in percentage was calculated as:

$$\text{Diameter variation } [\%] = \frac{d_{pp} - d_{lp}}{d_{lp}} 100 \tag{2.7}$$

where d_{pp} is the area of the cross-section at peak pressure and d_{lp} is the area of the cross-section at the minimum pressure during the cardiac cycle. Since cross-sections S1 and S2 are not circular (Fig. 3) because of the presence of the stent struts, the hydraulic diameter was calculated for these locations as:

$$d_h = \frac{4A}{p} \tag{2.8}$$

where A is the area of the cross-section and p is its wetted perimeter.

To compare the FSI and rigid-wall models, the wall shear stress (WSS) and the time-averaged WSS (TAWSS) were considered. TAWSS is defined as:

$$\text{TAWSS} = \frac{1}{T} \int_0^T |\vec{\tau}_w| dt \tag{2.9}$$

where $\vec{\tau}_w$ is the WSS vector and T is the duration of one cardiac cycle. Low values of WSS have been recognized as critical for NH. Endothelial cells subjected to WSS lower than 0.4 Pa or oscillatory WSS are circular in shape without any preferred flow alignment pattern (Malek et al., 1999). These cells, coupled with the blood stagnation usually observed in regions of low WSS, lead to increased uptake of blood-borne particles to the arterial wall, which is prevalent in atherosclerosis, as a result of increased residence time and increased permeability of the endothelial layer (Murphy and Boyle, 2012). An inverse relationship between WSS magnitude and the extent of ISR was found both by *in vivo* animal studies (Carlier et al., 2003; LaDisa et al., 2005) and human studies (Gijsen et al., 2003; Papafaklis et al., 2009, 2007; Sanmartín et al., 2006; Thury et al., 2002; Wentzel et al., 2001).

WSS and TAWSS were analyzed in the region of the fluid-structure interface that contains the stent (in the following, we refer to it as the 'region of interest' (ROI); Fig. 3). In particular, the percentage area exposed to low

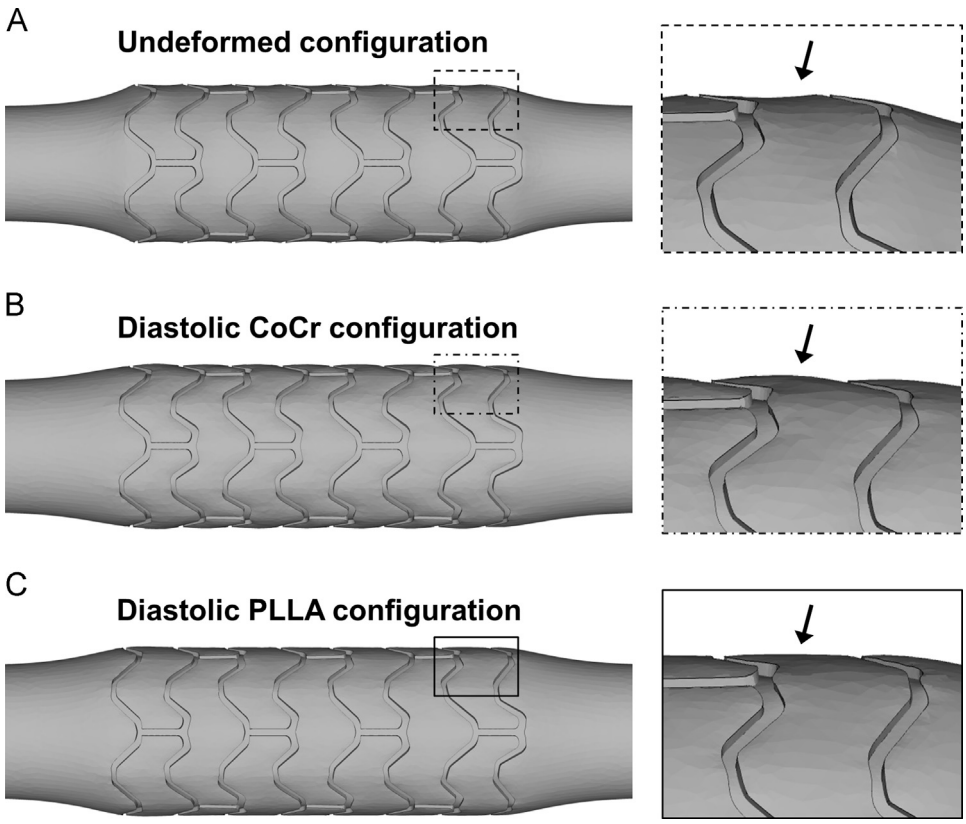

Fig. 2 – (A) Initial undeformed configuration of the FSI simulations, before the pressurization step. This configuration is identical for both CoCr and PLLA FSI cases. (B) Diastolic CoCr configuration. (C) Diastolic PLLA configuration. In the magnification boxes on the right, the tissue between two rings of the stent is shown. As indicated by the black arrows, in the undeformed configuration the tissue is prolapsed between the struts toward the interior of the vessel while in the diastolic configurations it is prolapsed toward the exterior for the effect of the blood pressure.

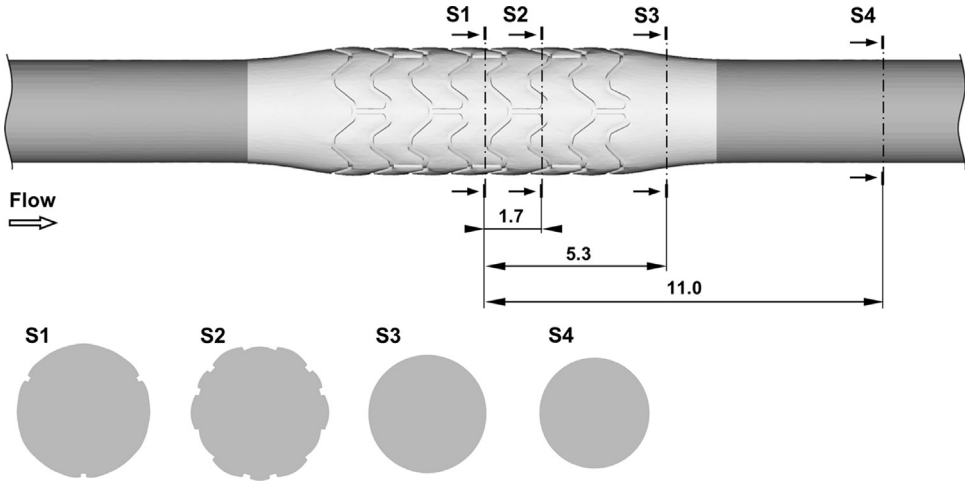

Fig. 3 – Location of the four cross-sections that were chosen to evaluate the variation of area and the corresponding diameter during the cardiac cycle. The region of interest (ROI) for the analysis of the WSS (region of the fluid-structure interface that contains the stent) is representated in light gray.

WSS was calculated in the ROI as the ratio between the area exposed to WSS lower than 0.4 Pa and the total area of the ROI. The area distribution of WSS was also visualized using histograms by displaying the amount of area of the ROI contained between specific intervals of the variable value (Murphy and Boyle, 2010b).

3. Results and discussion

The displacements of the fluid–structure interface that occur during the cardiac cycle for the two FSI models were first analyzed. The maximum displacements take place at peak pressure ($t=0.37$ s, $p=139.6$ mmHg); they are localized in the arterial wall portions immediately before and after the stent (Fig. 4a) and they are equal to 0.215 mm and 0.240 mm, respectively for case FSI CoCr and FSI PLLA. A qualitative comparison of the contour maps of displacement magnitude shown in Fig. 4a highlights the different influence of the CoCr and PLLA stents on the arterial wall deformation: CoCr struts do not move as a consequence of the blood pressure variation; only the arterial wall portions within the stent cell dilate. On the contrary, PLLA struts, with a Young's modulus of two orders of magnitude lower than the CoCr, significantly move; the displacement value is between 0.09 mm and 0.15 mm in all the stented region. The same behavior is evident looking at the displacements on a line in the axial direction of the vessel for the two FSI cases (Fig. 4b).

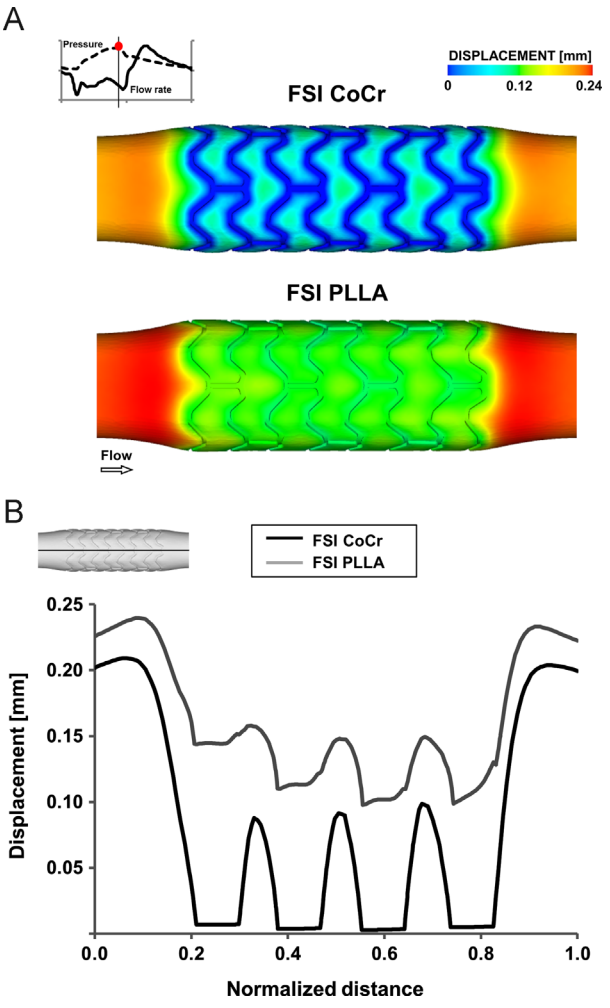

Fig. 4 – (A) Contour maps of displacement magnitude along the fluid–structure interface of case FSI CoCr (top) and FSI PLLA (bottom) at peak pressure (t=0.37 s, $p=139.6$ mmHg), in the region of interest (ROI). (B) Displacements on a line in the axial direction of the vessel for the cases FSI CoCr and PLLA at peak pressure. The distance is normalized in the ROI. The reference line is shown on the top left image of the vessel model. (For interpretation of the references to color in this figure legend, the reader is referred to the web version of this article.)

The variation of area and the corresponding diameter of the four cross-sections chosen for the FSI models are reported in Table 1. These data confirms the rigid behavior of the CoCr stent. The cross-sections characterized by the presence of the stent struts (S1 and S2) show lower area and diameter variations if compared to the cross-sections outside the stented region (S3 and S4). In particular, S2, which is characterized by the higher amount of struts, has the lowest area and diameter variation, 0.47% and 0.11%, respectively. Cross-sections S3 and S4 have values of area and diameter variations comparable to the FSI PLLA model, about 4.3% and 2.1%, respectively. The FSI PLLA case shows a more uniform behavior than the FSI CoCr case, with similar values of area and diameter variations for all the analyzed cross-sections.

The values of diameter variation outside the stented region (S3 and S4) can be compared to literature data. The values are similar to those found by Malvè et al. (2012) and Torii et al. (2009) with their FSI models of coronary arteries. Moreover, the FSI simulations of the present study show comparable values of diameter variation to the experimental findings by Schaar et al. (2005) based on IVUS palpography measurements. The values of area variation outside the stented region are in accordance with those reported for patients with coronary artery disease by Kelle et al. (2011) (mean area change equal to 2.9 %, calculated using angiography, and to 5.3 %, using magnetic resonance imaging) and by Peters et al. (1996) and Weissman et al. (1995) (range from 2.0 % to 5.9 %, calculated using IVUS).

As previously shown by experimental and computational studies (Haluska et al., 2007; Tada and Tarbell, 2005), the temporal variation of vessel diameters is in phase with the pressure.

In order to study the effects of the wall compliance on the hemodynamics of a coronary stented artery model, the WSS patterns were analyzed. In Fig. 5 the contour maps of TAWSS along the fluid–structure interface for the FSI and rigid-wall cases are depicted. Low TAWSS are located next to the stent struts. For each repeating stent cell, the values of TAWSS increase from the zones near the struts towards the center of each cell. These findings are in agreement with several previous computational studies (Balossino et al., 2008; Duraiswamy et al., 2008; Gundert et al., 2013). A qualitative comparison of the contour maps of both the CoCr and PLLA cases does not point out any significant difference between the FSI and rigid-wall models. In Fig. 6 the TAWSS on a line in the axial direction of the vessel is displayed for the CoCr and PLLA cases. The values of TAWSS are slightly higher in the FSI model in the portions of the fluid–structure interface outside the stent, while they are similar in the vicinity of the struts. This means that the stent makes the vessel wall stiffer, thus reducing the WSS differences.

The percentage area exposed to TAWSS lower than 0.4 Pa in the ROI (Table 2) is similar between the FSI and rigid-wall cases. In particular, the percentage difference between the CoCr FSI and rigid-wall cases is equal to 1.57% while between the PLLA cases is 1.05%.

Table 1 – Variations of area and diameter of the four analyzed locations of FSI CoCr and FSI PLLA models.

Location	Area variation [mm^2]		Area variation [%]		Diameter variation [mm]		Diameter variation [%]	
	FSI CoCr	FSI PLLA	FSI CoCr	FSI PLLA	FSI CoCr	FSI PLLA	FSI CoCr	FSI PLLA
S1	0.802	3.948	0.86	4.07	0.013	0.071	0.41	2.12
S2	0.418	3.975	0.47	4.23	0.003	0.071	0.11	2.32
S3	3.051	3.370	4.32	4.42	0.064	0.068	2.14	2.19
S4	2.653	2.587	4.31	4.20	0.060	0.058	2.13	2.08

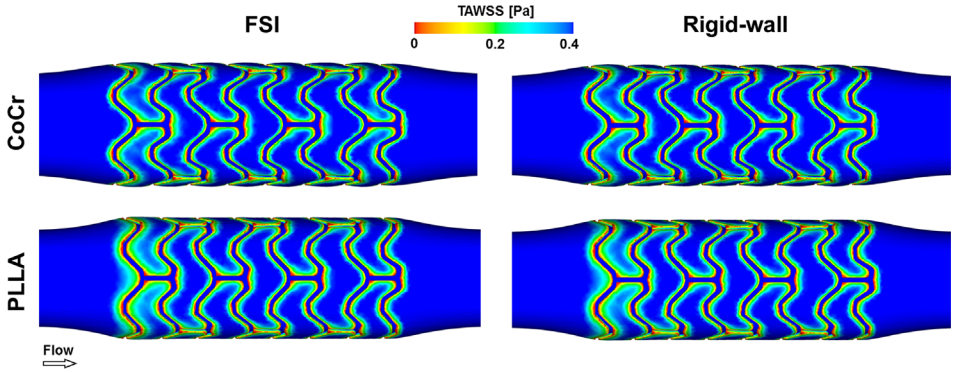

Fig. 5 – Contour maps of TAWSS along the fluid-structure interface: (left) CoCr and PLLA FSI models; (right) CoCr and PLLA rigid-wall models. Low TAWSS are indicated in red. (For interpretation of the references to color in this figure legend, the reader is referred to the web version of this article.)

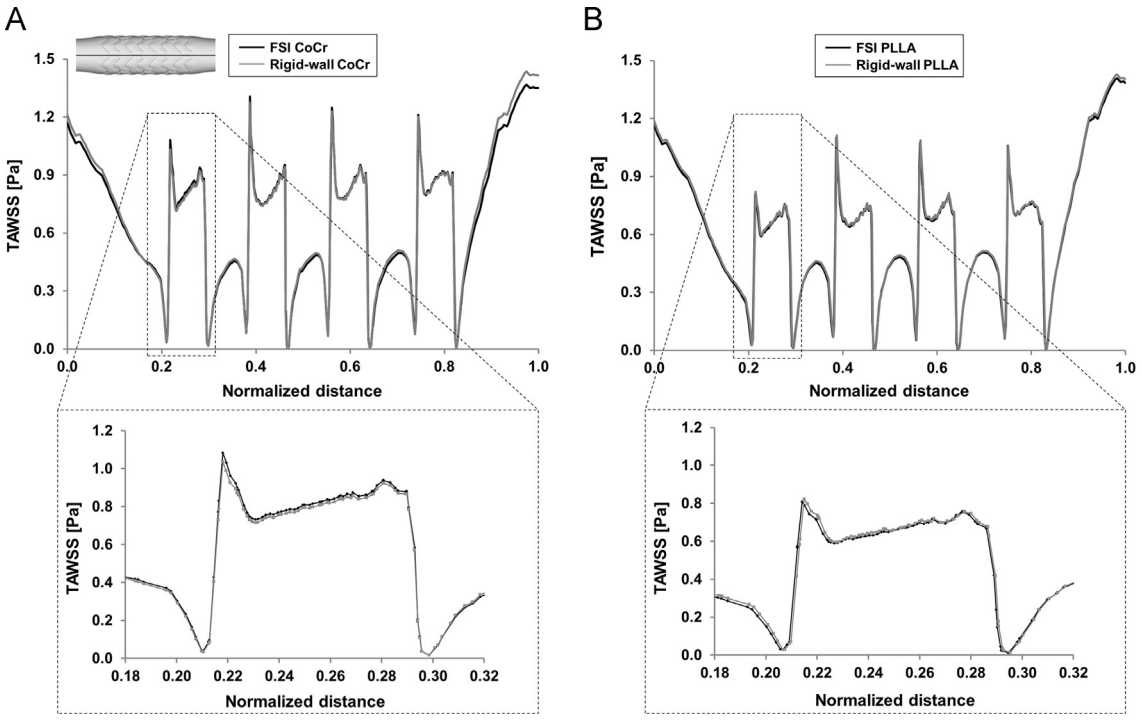

Fig. 6 – TAWSS on a line in the axial direction of the vessel: (A) FSI and rigid-wall CoCr models; (B) FSI and rigid-wall PLLA models. The distance is normalized in the region of interest (ROI). The reference line is shown on the top left image. In the magnification area, an example of WSS peaks due to the presence of stent struts is displayed.

In Fig. 7 the area distribution of TAWSS in the ROI are presented for the four analyzed cases. To better visualize the differences between the histograms, the bars with an absolute difference greater than 0.005 between the FSI and rigid-wall models are indicated by symbols. Differences between the bars are small: the maximum absolute difference for the CoCr cases is 0.022 (interval 1.4–1.5 Pa) while for the PLLA cases is 0.008 (interval 1.4–1.5 Pa).

In addition to the TAWSS, which is an average quantity, the instantaneous WSS were studied. The time instants corresponding to peak pressure and peak flow rate ($t=0.59$ s, $Q=91.1$ mL/min) were chosen. In Figs. 8 and 9 the distributions of WSS in the ROI are presented, respectively at peak pressure and flow rate. No significant differences between FSI and rigid-wall models can be detected, also considering the instantaneous quantities.

3.1. *Limitations*

Although this study proposes a novel aspect of the comparison between a stented artery analyzed under FSI and rigid-wall approach, some necessary assumptions were adopted.

The velocity and pressure waveforms imposed as boundary conditions of the models were taken from *in-vivo* data (Davies et al., 2006). Therefore, flow conditions are quite reliable. However, the heart motion, typical of the diastolic coronary flow, was neglected in this work, isolating the effects of the pure coronary artery intravascular flow on the wall compliance. The motion of coronary arteries can be described by overall vessel translation, stretching, bending and twisting and to a minor degree by radial expansion and axial torsion (Ramaswamy et al., 2004). The effects on hemodynamics in presence of the heart motion are still a subject of study. Several works have been proposed in the literature with conflicting results. In particular, Zeng et al. (2003) studied the hemodynamics of a RCA model under physiologically realistic cardiac-induced motion. These authors concluded that the motion effects were small compared to flow pulsation effects. Ramaswamy et al. (2004) found that arterial motion substantially affects the hemodynamics in the LAD. Prosi et al. (2004) considered a realistic curved model of the LAD with its first diagonal branch by attaching it to the surface of a sphere with time-varying radius based on experimental dynamic curvature data. Their results showed that the effect of curvature dynamics on the flow field were negligible. Theodorakakos et al. (2008)

Table 2 – Percentage of area exposed to WSS lower than 0.4 Pa in the region of interest (ROI).

	Percentage area with WSS < 0.4 Pa [%]			
	CoCr		PLLA	
Time instant	FSI	Rigid-wall	FSI	Rigid-wall
$t=0.37$ s	67.68	66.41	70.96	69.85
$t=0.59$ s	12.58	12.79	16.10	15.68
Time averaged	40.22	38.65	44.91	43.86

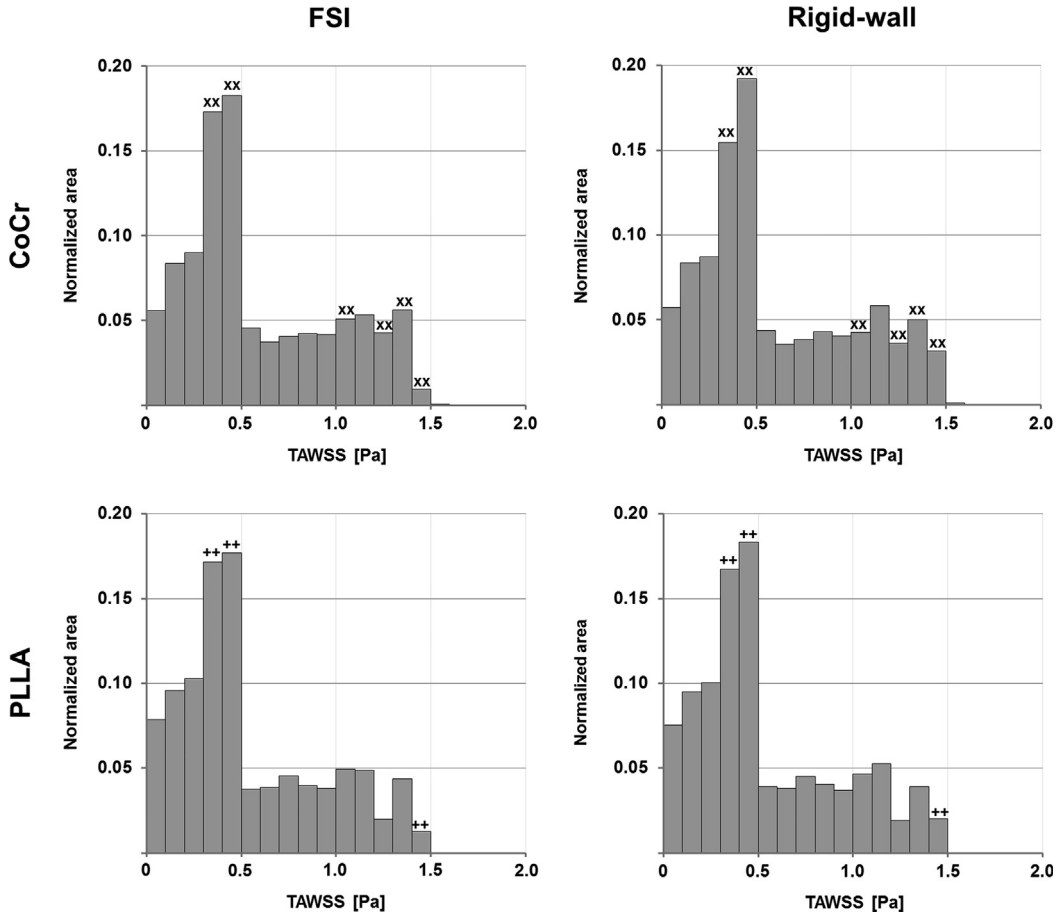

Fig. 7 – TAWSS distributions: (left) CoCr and PLLA FSI models; (right) CoCr and PLLA rigid-wall models. Each bar of the histograms represents the amount of normalized area with a defined range of TAWSS. Bar widths are 0.1 Pa. The bars with an absolute difference greater than 0.005 between the FSI and rigid-wall models are indicated by the symbols "xx" and "++", respectively for the CoCr and PLLA cases.

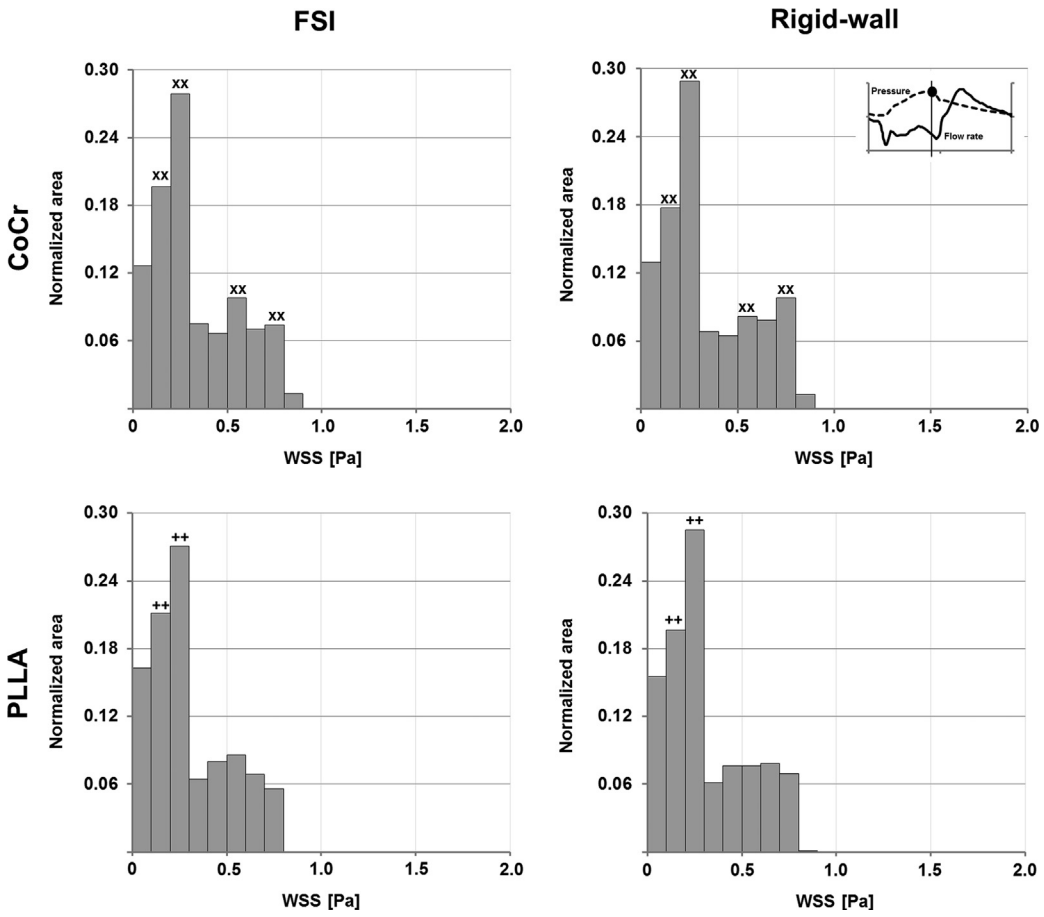

Fig. 8 – WSS distributions at peak pressure ($t=0.37$ s, $p=139.6$ mmHg): (left) CoCr and PLLA FSI models; (right) CoCr and PLLA rigid-wall models. Each bar of the histograms represents the amount of normalized area with a defined range of TAWSS. Bar widths are 0.1 Pa. The bars with an absolute difference greater than 0.01 between the FSI and rigid-wall models are indicated by the symbols "xx" and "++", respectively for the CoCr and PLLA cases.

studied the effect of myocardial motion on the flow field and WSS distribution of an imaged-based human LAD and its main branches in the presence of a stenosis. Results indicated that fluid dynamics was considerably affected by the pulsatile nature of the flow and myocardial motion had only a minor effect on flow patterns within the arterial tree. Although the absolute values of WSS were different, the WSS spatial distribution was very similar between the stationary and the moving coronary tree. Hasan et al. (2013) investigated the effects of cyclic motion (i.e. bending and stretching) on blood flow in a 3D model of a segment of the LAD, which was created on the basis of anatomical studies. Their results highlighted that, although the motion of the coronary artery could significantly affect blood particle trajectory, it had slight effect on velocity and WSS.

The second assumption of this work is related to the modeling of the arterial wall, which was considered as a hyperelastic incompressible isotropic and homogeneous material using the strain energy function originally proposed by Demiray (1972). A more realistic model for the material might be implemented taking into account the anisotropy related to collagen fiber dispersion in the tissue (Gasser et al., 2006) and the three-layered characterization of the arterial wall (Holzapfel et al., 2005). Moreover, the initial stresses due to the stent deployment were neglected in this preliminary study. In fact, in the current version of the used software, the influence of the aforementioned stresses cannot be taken into account. This aspect may over-estimate the computation of the displacements in the arterial wall.

Lastly, the initial structural simulation of stent deployment was used exclusively to obtain the geometry for the subsequent FSI and rigid-wall fluid dynamic simulations. The stress state of the artery and the stent due to the expansion of the device were not considered in the FSI analyses. Therefore, the stress in the artery and in the stent calculated in these analyses might be underestimated. Even though this approximation may strongly affect the wall stresses and strains computation, the compliance, which was evaluated in this study, is relatively unaffected, depending basically only on the pressure field.

4. Conclusions

A FSI model of an idealized straight stented coronary artery was created and compared to the corresponding rigid-wall model in order to understand the effects of the wall compliance on the hemodynamics. The effect of two different stent materials, CoCr and PLLA, on the results was evaluated.

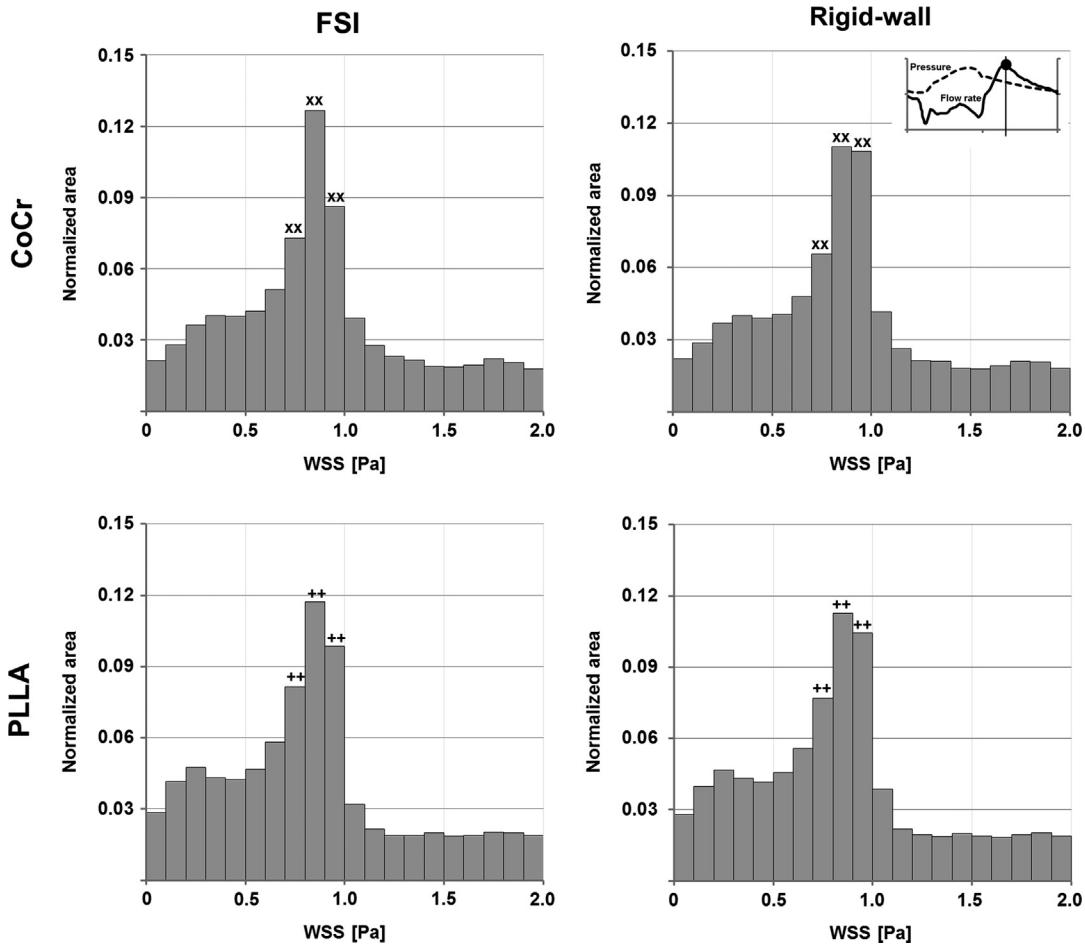

Fig. 9 – WSS distributions at peak flow rate ($t=0.59$ s, $Q=91.1$ mL/min): (left) CoCr and PLLA FSI models; (right) CoCr and PLLA rigid-wall models. Each bar of the histograms represents the amount of normalized area with a defined range of TAWSS. Bar widths are 0.1 Pa. The bars with an absolute difference greater than 0.01 between the FSI and rigid-wall models are indicated by the symbols "xx" and "++", respectively for the CoCr and PLLA cases.

Similar results were found in terms of TAWSS and instantaneous WSS between compliant and rigid-wall cases: the contour maps of WSS and also the WSS profiles are qualitatively similar; the difference of percentage area exposed to TAWSS lower than 0.4 Pa in the stented region between the FSI and the rigid-wall cases is low (about 1.5% and 1.0%, respectively for the CoCr and PLLA cases). The comparison between compliant and rigid-wall cases showed similar results in terms of WSS although CoCr and PLLA FSI models deforms differently during the cardiac cycle, with higher values of displacement in the stented region for the PLLA FSI case.

The results of the present work indicate that, for idealized models of a stented coronary artery, the rigid-wall assumption for fluid dynamic simulations appears adequate when the aim of the study is the analysis of near-wall quantities like WSS.

Acknowledgments

The authors would like to acknowledge Stefano Morlacchi, PhD (Laboratory of Biological Structure Mechanics (LaBS), Department of Chemistry, Materials and Chemical Engineering "Giulio Natta", Politecnico di Milano, Italy) for the initial structural simulation of stent deployment.

The support of Dr. Jingping Long and Dr. Jianghui Chao of the Adina Support (Adina R&D, Watertown, MA, USA) is highly appreciated.

Mauro Malvè and Miguel Angel Martínez are supported by the research project DPI2010-20746-C03-01 of the Spanish Ministry od Science and Tecnology.

Francesco Migliavacca and Claudio Chiastra are partially supported by the project "RT3S- Real Time Simulation for Safer vascular Stenting" funded by the European Commission under the 7th Framework Programme, GA FP7-2009-ICT-4-248801.

REFERENCES

Asanuma, T., Higashikuni, Y., Yamashita, H., Nagai, R., Hisada, T., Sugiura, S., 2013. Discordance of the areas of peak wall shear stress and tissue stress in coronary artery plaques as revealed by fluid-structure interaction finite element analysis: a case study. Int. Heart J. 54, 54–58, http://dx.doi.org/10.1536/ihj.54.54.

Balossino, R., Gervaso, F., Migliavacca, F., Dubini, G., 2008. Effects of different stent designs on local hemodynamics in stented

arteries. J. Biomech. 41, 1053–1061, http://dx.doi.org/10.1016/j.jbiomech.2007.12.005.
Bathe, K.J., 2006a. Theory and Modeling guide, vol. I: ADINA Solids & Structures, ADINA R&D, Inc., Watertown, MA, USA.
Bathe K.J., 2006b. Theory and Modeling guide, vol. II: ADINA CFD & FSI, ADINA R&D, Inc., Watertown, MA, USA.
Bathe, K.J., Zhang, H, 2004. Finite element developments for general fluid flows with structural interactions. Int. J. Numer. Methods Eng. 60, 213–232, http://dx.doi.org/10.1002/nme.959.
Bathe, K.J., Zhang, H., Ji, S., 1999. Finite element analysis of fluid flows fully coupled with structural interactions. Comput. Struct. 72, 1–16.
Belzacq, T., Avril, S., Leriche, E., Delache, A., 2012. A numerical parametric study of the mechanical action of pulsatile blood flow onto axisymmetric stenosed arteries. Med. Eng. Phys. 34, 1483–1495, http://dx.doi.org/10.1016/j.medengphy.2012.02.010.
Carlier, S.G., van Damme, L.C., Blommerde, C.P., Wentzel, J.J., van Langehove, G., Verheye, S., Kockx, M.M., Knaapen, M.W., Cheng, C., Gijsen, F., Duncker, D.J., Stergiopulos, N., Slager, C.J., Serruys, P.W., Krams, R., 2003. Augmentation of wall shear stress inhibits neointimal hyperplasia after stent implantation: inhibition through reduction of inflammation?. Circulation 107, 2741–2746, http://dx.doi.org/10.1161/01.CIR.0000066914.95878.6D.
Carmines, D., McElhaney, J., Stack, R., 1991. A piece-wise nonlinear elastic stress expression of human and pig coronary-arteries tested in vitro. J. Biomech. 24, 899–906, http://dx.doi.org/10.1016/0021-9290(91)90168-M.
Chiastra, C., Morlacchi, S., Gallo, D., Morbiducci, U., Cárdenes, R., Larrabide, I., Migliavacca, F., 2013. Computational fluid dynamic simulations of image-based stented coronary bifurcation models. J. R. Soc. Interface 10, 20130193, http://dx.doi.org/10.1098/rsif.2013.0193.
Chiastra, C., Morlacchi, S., Pereira, S., Dubini, G., Migliavacca, F., 2012. Fluid dynamics of stented coronary bifurcations studied with a hybrid discretization method. Eur. J. Mech. – B/Fluids 35, 76–84, http://dx.doi.org/10.1016/j.euromechflu.2012.01.011.
Davies, J.E., Whinnett, Z.I., Francis, D.P., Manisty, C.H., Aguado-Sierra, J., Willson, K., Foale, R.A., Malik, I.S., Hughes, A.D., Parker, K.H., Mayer, J., 2006. Evidence of dominant backward-propagating suction wave responsible for diastolic coronary filling in humans, attenuated in left ventricular hypertrophy. Circulation 113, 1768–1778, http://dx.doi.org/10.1161/CIRCULATIONAHA.105.603050.
Delfino, A., Stergiopulos, N., Moore Jr., J.E., Meister, J.-J., 1997. Residual strain effects on the stress field in a thick wall finite element model of the human carotid bifurcation. J. Biomech. 30, 777–786, http://dx.doi.org/10.1016/S0021-9290(97)00025-0.
Demiray, H, 1972. A note on the elasticity of biological soft tissues. J. Biomech. 5, 309–311, http://dx.doi.org/10.1016/0021-9290(72)90047-4.
Donea, J., Giuliani, S., Halleux, J.P., 1982. An arbitrary Lagrangian–Eulerian finite element method for transient dynamic fluid-structure interaction. Comput. Methods Appl. Mech. Eng. 33, 689–723, http://dx.doi.org/10.1016/0045-7825(82)90128-1.
Duraiswamy, N., Cesar, J.M., Schoephoerster, R.T., Moore Jr., J.E., 2008. Effects of stent geometry on local flow dynamics and resulting platelet deposition in an in vitro model. Biorheology 45, 547–561, http://dx.doi.org/10.3233/BIR-2008-0497.
Ellwein, L.M., Otake, H., Gundert, T.J., Koo, B., Shinke, T., Honda, Y., Shite, J., LaDisa Jr., J.F., 2011. Optical coherence tomography for patient-specific 3D artery reconstruction and evaluation of wall shear stress in a left circumflex coronary artery. Cardiovasc. Eng. Technol. 2, 212–227 http://dx.doi.org/10.1007/s13239-011-0047-5.
Figueroa, C.A., Vignon-Clementel, I.E., Jansen, K.E., Hughes, T.J.R., Taylor, C.A., 2006. A coupled momentum method for modeling blood flow in three-dimensional deformable arteries. Comput. Methods Appl. Mech. Eng. 195, 5685–5706, http://dx.doi.org/10.1016/j.cma.2005.11.011.
Filipovic, N., Teng, Z., Radovic, M., Saveljic, I., Fotiadis, D., Parodi, O., 2013. Computer simulation of three-dimensional plaque formation and progression in the carotid artery. Med. Biol. Eng. Comput. 51, 607–616, http://dx.doi.org/10.1007/s11517-012-1031-4.
Gao, H., Long, Q., Graves, M., Gillard, J.H., Li, Z.Y., 2009. Carotid arterial plaque stress analysis using fluid-structure interactive simulation based on in-vivo magnetic resonance images of four patients. J. Biomech. 42, 1416–1423, http://dx.doi.org/10.1016/j.jbiomech.2009.04.010.
Gastaldi, D., Morlacchi, S., Nichetti, R., Capelli, C., Dubini, G., Petrini, L., Migliavacca, F., 2010. Modelling of the provisional side-branch stenting approach for the treatment of atherosclerotic coronary bifurcations: effects of stent positioning. Biomech. Model Mechanobiol. 9, 551–561, http://dx.doi.org/10.1007/s10237-010-0196-8.
Gasser, T.C., Ogden, R.W., Holzapfel, G.A., 2006. Hyperelastic modeling of arterial layers with distributed collagen fibre orientations. J. R. Soc. Interface 3, 15–35, http://dx.doi.org/10.1098/rsif.2005.0073.
Gerbeau, J.-F., Vidrascu, M., Frey, P., 2005. Fluid-structure interaction in blood flows on geometries based on medical imaging. Comput. Struct. 83, 155–165, http://dx.doi.org/10.1016/j.compstruc.2004.03.083.
Gijsen, F.J., Oortman, R.M., Wentzel, J.J., Schuurbiers, J.C., Tanabe, K., Degertekin, M., Ligthart, J.M., Thury, A., de Feyter, P.J., Serruys, P.W., Slager, C.J., 2003. Usefulness of shear stress pattern in predicting neointima distribution in sirolimus-eluting stents in coronary arteries. Am. J. Cardiol. 92, 1325–1328, http://dx.doi.org/10.1016/j.amjcard.2003.08.017.
Gundert, T.J., Dholakia, R.J., McMahon, D., LaDisa Jr., J.F., 2013. Computational fluid dynamics evaluation of equivalency in hemodynamic alterations between Driver, Integrity, and similar stents implanted into an idealized coronary artery. J. Med. Devices 7, 011004, http://dx.doi.org/10.1115/1.4023413.
Gundert, T.J., Marsden, A.L., Yang, W., Ladisa, J.F., 2012. Optimization of cardiovascular stent design using computational fluid dynamics. J. Biomech. Eng. 134, 011002, http://dx.doi.org/10.1115/1.4005542.
Gundert, T.J., Shadden, S.C., Williams, A.R., Koo, B., Feinstein, J.A., LaDisa Jr, J.F., 2011. Rapid and computationally inexpensive method to virtually implant current and next-generation stents into subject-specific computational fluid dynamics models. Ann. Biomed. Eng. 39, 1423–1436 http://dx.doi.org/10.1007/s10439-010-0238-5.
Haluska, B.A., Jeffriess, L., Mottram, P.M., Carlier, S.G., Marwick, T.H., 2007. A new technique for assessing arterial pressure wave forms and central pressure with tissue doppler. Cardiovasc. Ultrasound 5, 6, http://dx.doi.org/10.1186/1476-7120-5-6.
Hasan, M., Rubenstein, D., Yin, W., 2013. Effects of cyclic motion on coronary blood flow. J. Biomech. Eng. 135 (12), 121002, http://dx.doi.org/10.1115/1.4025335.
Hofer, M., Rappitsch, G., Perktold, K., Trubel, W., Schima, H., 1996. Numerical study of wall mechanics and fluid dynamics in end-to-side anastomoses and correlation to intimal hyperplasia. J. Biomech. 29, 1297–1308, http://dx.doi.org/10.1016/0021-9290(96)00036-X.
Holzapfel, G.A., Sommer, G., Gasser, C.T., Regitnig, P., 2005. Determination of layer-specific mechanical properties of human coronary arteries with nonatherosclerotic intimal thickening and related constitutive modeling. Am. J. Physiol. Heart Circ. Physiol. 289, H2048–H2058, http://dx.doi.org/10.1152/ajpheart.00934.2004.
Kelle, S., Hays, A., Hirsch, G., Gerstenblith, G., Miller, J., Steinberg, A., Schr, M., Texter, J., Wellnhofer, E., Weiss, R., Stuber, M.,

2011. Coronaryartery distensibility assessed by 3.0 Tesla coronary magnetic resonance imaging in subjects with and without coronary artery disease. Am. J. Cardiol. 108, 491–497, http://dx.doi.org/10.1016/j.amjcard.2011.03.078.

Koshiba, N., Ando, J., Chen, X., Hisada, T., 2007. Multiphysics simulation of blood flow and LDL transport in a porohyperelastic arterial wall model. J. Biomech. Eng. 129, 374–385, http://dx.doi.org/10.1115/1.2720914.

LaDisa Jr., J.F., Olson, L.E., Molthen, R.C., Hettrick, D.A., Pratt, P.F., Hardel, M.D., Kersten, J.R., Warltier, D.C., Pagel, P.S., 2005. Alterations in wall shear stress predict sites of neointimal hyperplasia after stent implantation in rabbit iliac arteries. Am. J. Physiol. Heart Circ. Physiol. 288, H2465–H2475, http://dx.doi.org/10.1152/ajpheart.01107.200.

Lee, S.H., Kang, S., Hur, N., Jeong, S.-K., 2012. A fluid-structure interaction analysis on hemodynamics in carotid artery based on patient-specific clinical data. J. Mech. Sci. Technol. 26, 3821–3831, http://dx.doi.org/10.1007/s12206-012-1008-0.

Leuprecht, A., Perktold, K., Prosi, M., Berk, T., Trubel, W., Schima, H., 2002. Numerical study of hemodynamics and wall mechanics in distal end-to-side anastomoses of bypass grafts. J. Biomech. 35, 225–236, http://dx.doi.org/10.1016/S0021-9290(01)00194-4.

Leung, J.H., Wright, A.R., Cheshire, N., Crane, J., Thom, S.A., Hughes, A.D., Xu, Y., 2006. Fluid structure interaction of patient specific abdominal aortic aneurisms: a comparison with solid stress models. Biomed. Eng. Online 5, 33, http://dx.doi.org/10.1186/1475-925X-5-33.

Malek, A.M., Alper, S.L., Izumo, S., 1999. Hemodynamic shear stress and its role in atherosclerosis. J. Am. Med. Assoc. 282, 2035–2042, http://dx.doi.org/10.1001/jama.282.21.2035.

Malvè, M., Chandra, S., García, A., Mena, A., Martínez, M.A., Finol, E.A., Doblaré, M., 2014. Impedance-based outflow boundary conditions for human carotid haemodynamics. Comput. Methods Biomech. Biomed. Eng. http://dx.doi.org/10.1080/10255842.2012.744396.

Malvè, M., García, A., Ohayon, J., Martínez, M.A., 2012. Blood flow and mass transfer of a human left coronary artery bifurcation: FSI vs. CFD. Int. Commun. Heat Mass 39, 745–751, http://dx.doi.org/10.1016/j.i.cheatmasstransfer.2012.04.009.

Morlacchi, S., Chiastra, C., Gastaldi, D., Pennati, G., Dubini, G., Migliavacca, F., 2011. Sequential structural and fluid dynamic numerical simulations of a stented bifurcated coronary artery. J. Biomech. Eng. 133, 121010, http://dx.doi.org/10.1115/1.4005476.

Murphy, E.A., Boyle, F.J, 2012. Reducing in-stent restenosis through novel stent flow field augmentation. Cardiovasc. Eng. Technol. 3, 353–373, http://dx.doi.org/10.1007/s13239-012-0109-3.

Murphy, J.B., Boyle, F.J., 2010a. Predicting neointimal hyperplasia in stented arteries using time-dependant computational fluid dynamics: a review. Comput. Biol. Med. 40, 408–418, http://dx.doi.org/10.1016/j.compbiomed.2010.02.005.

Murphy, J.B., Boyle, F.J., 2010b. A numerical methodology to fully elucidate the altered wall shear stress in a stented coronary artery. Cardiovasc. Eng. Technol. 1, 256–268, http://dx.doi.org/10.1007/s13239-010-0028-0).

Pant, S., Bressloff, N.W., Forrester, A.I.J., Curzen, N., 2010. The influence of strut-connectors in stented vessels: a comparison of pulsatile flow through five coronary stents. Ann. Biomed. Eng. 38, 1893–1907, http://dx.doi.org/10.1007/s10439-010-9962-0.

Papafaklis, M.I., Bourantas, C.V., Theodorakis, P.E., Katsouras, C.S., Fotiadis, D.I., Michalis, L.K., 2009. Relationship of shear stress with in-stent restenosis: bare metal stenting and the effect of brachytherapy. Int. J. Cardiol. 134, 25–32, http://dx.doi.org/10.1016/j.ijcard.2008.02.006.

Papafaklis, M.I., Katsouras, C.S., Theodorakis, P.E., Bourantas, C.V., Fotiadis, D.I., Michalis, L.K., 2007. Coronary dilatation 10 weeks after paclitaxel-eluting stent implantation. No role of shear stress in lumen enlargement?. Heart Vessels 22, 268–273, http://dx.doi.org/10.1007/s00380-006-0970-9.

Park, S.-J., Kang, S.-J., Virmani, R., Nakano, M., Ueda, Y., 2012. In-stent neoatherosclerosis: a final common pathway of late stent failure. J. Am. Coll. Cardiol. 59, 2051–2057, http://dx.doi.org/10.1016/j.jacc.2011.10.909.

Perktold, K., Rappitsch, G, 1995. Computer simulation of local blood flow and vessel mechanics in a compliant carotid artery bifurcation model. J. Biomech. 28, 845–856.

Peters, R., Kok, W., Rijsterborgh, H., Van Dijk, M., Koch, K., Piek, J., David, G., Visser, C., 1996. Reproducibility of quantitative measurements from intracoronary ultrasound images. beat-to-beat variability and influence of the cardiac cycle. Eur. Heart J. 17, 1593–1599.

Prosi, M., Perktold, K., Ding, Z., Friedman, M.H., 2004. Influence of curvature dynamics on pulsatile coronary artery flow in a realistic bifurcation model. J. Biomech. 37, 1767–1775, http://dx.doi.org/10.1016/j.jbiomech.2004.01.021.

Ramaswamy, S.D., Vigmostad, S.C., Wahle, A., Lai, Y.-G., Olszeski, M.E., Braddy, K.C., Brennan, T.M.H., Rossen, J.D., Sonka, M., Chandran, K.B., 2004. Fluid dynamic analysis in a human left anterior descending coronary artery with arterial motion. Ann. Biomed. Eng. 32, 1628–1641.

Rikhtegar, F., Pacheco, F., Wyss, C., Stok, K.S., Ge, H., Choo, R.J., Ferrari, A., Poulikakos, D., Müller, R., Kurtcuoglu, V., 2013. Compound ex vivo and in silico method for hemodynamic analysis of stented arteries. PLoS One 8, e58147, http://dx.doi.org/10.1371/journal.pone.0058147.

Rodriguez, J., Ruiz, C., Doblaré, M., Holzapfel, G., 2008. Mechanical stresses in abdominal aortic aneurysm: influence of diameter, asymmetry and material anisotropy. J. Biomech. Eng. 130, 1–10, http://dx.doi.org/10.1115/1.2898830.

Sanmartín, M., Goicolea, J., García, C., García, J., Crespo, A., Rodríguez, J., Goicolea, J.M., 2006. Influence of shear stress on in-stent restenosis: in vivo study using 3D reconstruction and computational fluid dynamics. Rev. Esp. Cardiol. 59, 20–27, http://dx.doi.org/10.1157/13083645.

Scotti, C.M., Jimenez, J., Muluk, S.C., Finol, E.A., 2008. Wall stress and flow dynamics in abdominal aortic aneurysms: Finite element analysis vs. fluid-structure interaction. Comput. Methods Biomech. Biomed. Eng 11, 301–322, http://dx.doi.org/10.1080/10255840701827412.

Scotti, C.M., Finol, E.A., 2007. Compliant biomechanics of abdominal aortic aneurysms: a fluid-structure interaction study. Comput. Struct. 85, 1097–1113, http://dx.doi.org/10.1016/j.compstruc.2006.08.041.

Schaar, J.A., De Korte, C.L., Mastik, F., Van Damme, L.C.A., Krams, R., Serruys, P.W., Van Der Steen, A.F.W., 2005. Three-dimensional palpography of human coronary arteries: Ex vivo validation and in-patient evaluation. Hertz 30, 125–133, http://dx.doi.org/10.1007/s00059-005-2642-4.

Spurk, J.H., Aksel, N, 2008. Fluid Mechanics, second ed. Springer-Verlag, Berlin Heidelberghttp://dx.doi.org/10.1007/978-3-540-73537-3.

Tada, S., Tarbell, J.M., 2005. A computational study of flow in a compliant carotid bifurcation-stress phase angle correlation with shear stress. Ann. Biomed. Eng. 33, 1202–1212, http://dx.doi.org/10.1007/s10439-005-5630-1.

Takizawa, K., Brummer, T., Tezduyar, T.E., Chen, P.R., 2012. A comparative study based on patient-specific fluid-structure interaction modeling of cerebral aneurysms. J. Appl. Mech. 79, 010908, http://dx.doi.org/10.1115/1.4005071.

Takizawa, K., Moorman, C., Wright, S., Purdue, J., McPhail, T., Chen, P.R., Warren, J., Tezduyar, T.E., 2011. Patient-specific arterial fluid-structure interaction modeling of cerebral aneurysms. Int. J. Numer. Meth. Fluids 65, 308–323, http://dx.doi.org/10.1002/fld.2360.

Tang, D., Yang, C., Mondal, S., Liu, F., Canton, G., Hatsukami, T.S., Yuan, C., 2008. A negative correlation between human carotid atherosclerotic plaque progression and plaque wall stress: In vivo MRI-based 2D/3D FSI models. J. Biomech. 41, 727–736, http://dx.doi.org/10.1016/j.jbiomech.2007.11.026.

Tang, D., Yang, C., Kobayashi, S., Ku, D.N., 2004. Effect of a lipid pool on stress/strain distributions in stenotic arteries: 3-D fluid-structure interactions (FSI) models. J. Biomech. Eng. 126, 363–370, http://dx.doi.org/10.1115/1.1762898.

Tang, D., Yang, C., Kobayashi, S., Ku, D.N., 2001. Steady flow and wall compression in stenotic arteries: a three-dimensional thick-wall model with fluid-wall interactions. J. Biomech. Eng. 123, 548–557, http://dx.doi.org/10.1115/1.1406036.

Tang, D., Yang, C., Ku, D.N., 1999. A 3-D thin wall model with fluid-structure interactions for blood flow in carotid arteries with symmetric and asymmetric stenosis. Comput. Struct. 72, 357–377, http://dx.doi.org/10.1016/S0045-7949(99)00019-X.

Teng, Z., Canton, G., Yuan, C., Ferguson, M., Yang, C., Huang, X., Zheng, J., Woodard, P.K., Tang, D., 2010. 3D critical plaque wall stress is a better predictor of carotid plaque rupture sites than flow shear stress: an in vivo MRI-based 3D FSI study. J. Biomech. Eng. 132, 031007, http://dx.doi.org/10.1115/1.4001028.

Tezduyar, T.E., Sathe, S., Cragin, T., Nanna, B., Conklin, B.S., Pausewang, J., Schwaab, M., 2007. Modelling of fluid-structure interactions with the space-time finite elements: arterial fluid mechanics. Int. J. Numer. Meth. Fluids 54, 901–922, http://dx.doi.org/10.1002/fld.1443.

Theodorakakos, A., Gavaises, M., Andriotis, A., Zifan, A., Liatsis, P., Pantos, I., Efstathopoulos, E., Katritsis, D., 2008. Simulation of cardiac motion on non-Newtonian, pulsating flow development in the human left anterior descending coronary artery. Phys. Med. Biol. 53 (18), 4875–4892, http://dx.doi.org/10.1088/0031-9155/53/18/002.

Thury, A., Wentzel, J.J., Vinke, R.V., Gijsen, F.J., Schuurbiers, J.C., Krams, R., de Feyter, P.J., Serruys, P.W., Slager, C.J., 2002. Images in cardiovascular medicine. Focal in-stent restenosis near step-up: roles of low and oscillating shear stress?. Circulation 105, e185–e187, http://dx.doi.org/10.1161/01.CIR.0000018282.32332.13.

Torii, R., Oshima, T., Kobayashi, K., Takagi, T., Tezduyar, T., 2010. Role of 0D peripheral vasculature model in fluid-structure interaction modeling of aneurysm. Comput. Mech. 46, 43–52, http://dx.doi.org/10.1007/s00466-009-0439-7al. 2010.

Torii, R., Oshima, T., Kobayashi, K., Takagi, T., Tezduyar, T., 2006. Fluid-structure interaction modeling of aneurysmal conditions with high and normal blood pressures. Comput. Mech. 38, 482–490, http://dx.doi.org/10.1007/s00466-006-0065-6al. 2010.

Torii, R., Wood, N.B., Hadjiloizou, N., Dowsey, A.W., Wright, A.R., Hughes, A.D., Davies, J., Francis, D.P., Mayet, J., Yang, G.-Z., Thom, S.A.McG., Xu, X.Y., 2009. Fluid-structure interaction analysis of a patient-specific right coronary artery with physiological velocity and pressure waveforms. Commun. Numer. Meth. Eng. 25, 565–580, http://dx.doi.org/10.1002/cnm.1231.

Weissman, N., Palacios, I., Weyman, A., 1995. Dynamic expansion of the coronary arteries: implications for intravascular ultrasound measurements. Am. Heart J. 130, 46–51.

Wentzel, J.J., Krams, R., Schuurbiers, J.C.H., Oomen, J.A., Kloet, J., Van Der Giessen, W.J., Serruys, P.W., Slager, C.J., 2001. Relationship between neointimal thickness and shear stress after wallstent implantation in human coronary arteries. Circulation 103, 1740–1745, http://dx.doi.org/10.1161/01.CIR.103.13.1740.

Wentzel, J.J., Gijsen, F.J.H., Schuurbiers, J.C.H., van der Steen, A.F.W., Serruys, P.W., 2008. The influence of shear stress on in-stent restenosis and thrombosis. EuroIntervention 4 (Supl. C), C27–C32.

Wolters, B.J.B.M., Rutten, M.C.M., Schurink, G.W.H., Kose, U., De Hart, J., Van De Vosse, F.N., 2005. A patient-specific computational model of fluid–structure interaction in abdominal aortic aneurysms. Med. Eng. Phys. 27, 871–883, http://dx.doi.org/10.1016/j.medengphy.2005.06.008.

Yang, C., Canton, G., Yuan, C., Ferguson, M., Hatsukami, T.S., Tang, D., 2011. Impact of flow rates in a cardiac cycle on correlations between advanced human carotid plaque progression and mechanical flow shear stress and plaque wall stress. Biomed. Eng. Online 10, 61, http://dx.doi.org/10.1186/1475-925X-10-61.

Yang, C., Canton, G., Yuan, C., Ferguson, M., Hatsukami, T.S., Tang, D., 2010. Advanced human carotid plaque progression correlates positively with flow shear stress using follow-up scan data: an in vivo MRI multi-patient 3D FSI study. J. Biomech. 43, 2530–2538, http://dx.doi.org/10.1016/j.jbiomech.2010.05.018.

Yang, C., Bach, R.G., Zheng, J., Naqa, I.E., Woodard, P.K., Teng, Z., Billiar, K., Tang, D., 2009. In vivo IVUS-based 3-D fluid-structure interaction models with cyclic bending and anisotropic vessel properties for human atherosclerotic coronary plaque mechanical analysis. IEEE Trans. Biomed. Eng. 56, 2420–2428, http://dx.doi.org/10.1109/TBME.2009.2025658.

Zeng, D., Ding, Z., Friedman, M.H., Ethier, C.R., 2003. Effects of cardiac motion on right coronary artery hemodynamics. Ann. Biomed. Eng. 31, 420–429.